Turning On TTA: Tuning the Energy Landscape by Intermolecular Coupling

Colette M. Sullivan and Lea Nienhaus*

Department of Chemistry and Biochemistry, Florida State University, Tallahassee, FL 32306, USA

*Corresponding Author: lnienhaus@fsu.edu

ABSTRACT

The development of efficient solid-state photon upconversion (UC) devices remains paramount for practical applications of the technology. In recent years, incorporation of perovskite thin films as triplet sensitizers for triplet-triplet annihilation (TTA) based UC has provided a promising solution. In the pursuit of finding an 'ideal annihilator' to maximize the apparent anti-Stokes shift, we investigate naphtho[2,3-a]pyrene (NaPy) as an annihilator in both solution-based and perovskite-sensitized TTA-UC systems. Surprisingly, we observe different emission behavior of NaPy in the solid state based on the excitation wavelength. Under direct excitation, a high energy transition S₁' dominates the emission spectrum, while UC results in increased emission from a lower lying state S₁". We propose that this is the result of aggregation-related lowering of the singlet excited state thus changing the fundamental energic landscape underlying TTA. Aggregation decreases the singlet energy below the energy level of the triplet pair state ¹(TT), yielding energetically favorable emission from the aggregated singlet state S₁" and weak emission from the higher lying singlet state S₁' through thermally or entropically-driven TTA-UC.

INTRODUCTION

Charge transfer at the bulk lead halide perovskite/organic semiconductor (OSC) interface has proven useful in generating spin-triplet excitons in OSCs for photon upconversion (UC) via triplet-triplet annihilation (TTA). 1-5 While the majority of solid-state UC work to date has focused on rubrene, 4,6-11 recent work has shown that triplet generation via charge transfer at the perovskite/OSC is not limited in nature to rubrene, rather is a universal process enabled by a favorable energetic alignment of the conduction band (CB) and valence band (VB) with the triplet energy level. ¹² Due to the small achievable apparent anti-Stokes shift between the perovskite bandgap (1.55 eV) and the OSC emission (2.05 eV for rubrene doped with DBP, 2.19 eV undoped), new annihilators are required to increase the energy gain during UC. Many common solution-based annihilators such as 9,10-diphenylanthracene (DPA) struggle with excimer formation or other undesired aggregation-related effects in solid state, ¹³ leading to their use in e.g., hybrid solid/solution approaches as in a recent study by Schmidt and coworkers. 14 Another ubiquitous approach is to use DPA derivatives that prevent aggregation by addition of bulky substituents. 15-17 Using the anthracene derivative 1-chloro-9,10-bis(phenylethynyl)anthracene (1-CBPEA), our recent work has expanded the spectral region covered in perovskite-sensitized solid-state UC, yielding green upconverted emission at 550 nm (2.25 eV).¹² However, considering the 1.55 eV bandgap of the lead iodide perovskite sensitizer, 11,18-21 the ideal annihilator would have a triplet energy of ~1.5 eV, yielding the optimal upconverted emission at ~3.0 eV while still allowing for a small driving force for the electron/hole transfer underlying triplet generation. Here, naphtho[2,3-a]pyrene (NaPy) is introduced as a possible candidate for further extending the achievable energy gain during UC. NaPy has been previously investigated at the single molecule level using scanning tunneling microscopy, ^{22–24} and as a sky-blue dopant dye in organic light emitting devices. ^{25,26} However, to date, NaPy has not been utilized as an annihilator within TTA-UC systems. A previous report by Aggarwal et al. implies that NaPy is a singlet fission (SF) material with an ensemble triplet energy (T₁ = 1.23 eV) at less than half of the singlet energy S₁, which forms non-emissive J-aggregates in the solid state.27

Our results show that NaPy is a successful annihilator in both solution as well as in solid-state UC devices, indicating that its triplet energy T₁ must be equal to or higher than half the singlet energy S₁, or that the singlet state can be achieved by ambient thermal energy or entropically-driven processes.^{28,29} Surprisingly, our results show that the nature of the emissive state is dependent on the pathway through which the singlet state is achieved since the emission exhibits a different branching ratio of the emissive species upon direct emission and UC. However, the radiative relaxation from the emissive singlet excited state should not be sensitive to the pathway that is generated by, except, if different species are emitting under the different conditions, or if the true singlet excited state is not achieved in TTA-UC.

This suggests that different states in the OSC are emitting under direct excitation vs. after TTA-UC, which may be due to variations in the local environment of the molecules tuning the underlying energy landscape or changes in rate of TTA due to increased electronic coupling.⁸ For example, Gray $et\ al$. have shown that conformational flexibility of the phenylethynyl arms in 9,10-bis(phenylethynyl)anthracene (BPEA) results in a change in the energy surface of the singlet and triplet energy manifold voiding the main requirement for TTA-UC: $E(S_1) \lesssim 2\ E(T_1)$.³⁰

Translating this previous insight to the NaPy study presented here, the underlying inhomogeneity in the OSC film can result in either: i) a change in the charge extraction rate and yield in triplet formation at the perovskite/OSC interface due to a change in the electronic coupling based on the molecular orientation. ii) A change in the rate of TTA due to variations in the intermolecular coupling strength,³¹ which has previously also been observed in the reverse process of SF.^{32,33} Or, iii) aggregation-based lowering of the singlet energy level, resulting in preferential TTA-UC to the aggregate singlet energy level.

RESULTS AND DISCUSSION

To elucidate the photophysical properties of this system, first, NaPy is characterized as a solution in toluene. Figure 1a shows the absorption and photoluminescence (PL) spectra of NaPy at a concentration of 150 μ M. The singlet energy level of the NaPy monomer is extracted at $S_1 = 2.66$ eV. Reminiscent of the transient absorption (TA) spectroscopy of rubrene,³⁴ TA of the NaPy solution yields a strong singlet-related excited

state absorption (ESA) $S_1 \rightarrow S_n$ which overlaps and dominates the expected spectral region of the ground state bleach (Figure 1b). However, as indicated previously, here, NaPy is investigated as a triplet annihilator. To further pinpoint the triplet energy level in this molecule, zinc octaethylporphyrin (ZnOEP, $T_1 = 1.78$ eV)³⁰ is utilized to sensitize the triplet state of NaPy in solution. As shown in Figure 1c, upconverted PL is successfully observed under 532 nm excitation. However, the successful observation of TTA-UC provides a lower bound of \sim 1.3 eV for the NaPy triplet energy T_1 in solution due to the fundamental energetic requirement of TTA-UC: $E(S_1) \lesssim 2 E(T_1)$, while the upper bound of the triplet energy is set by the ZnOEP triplet energy of 1.78 eV. This is in good agreement with the previous report of the triplet energy of the NaPy monomer: $T_1 < 1.37$ eV.²⁷

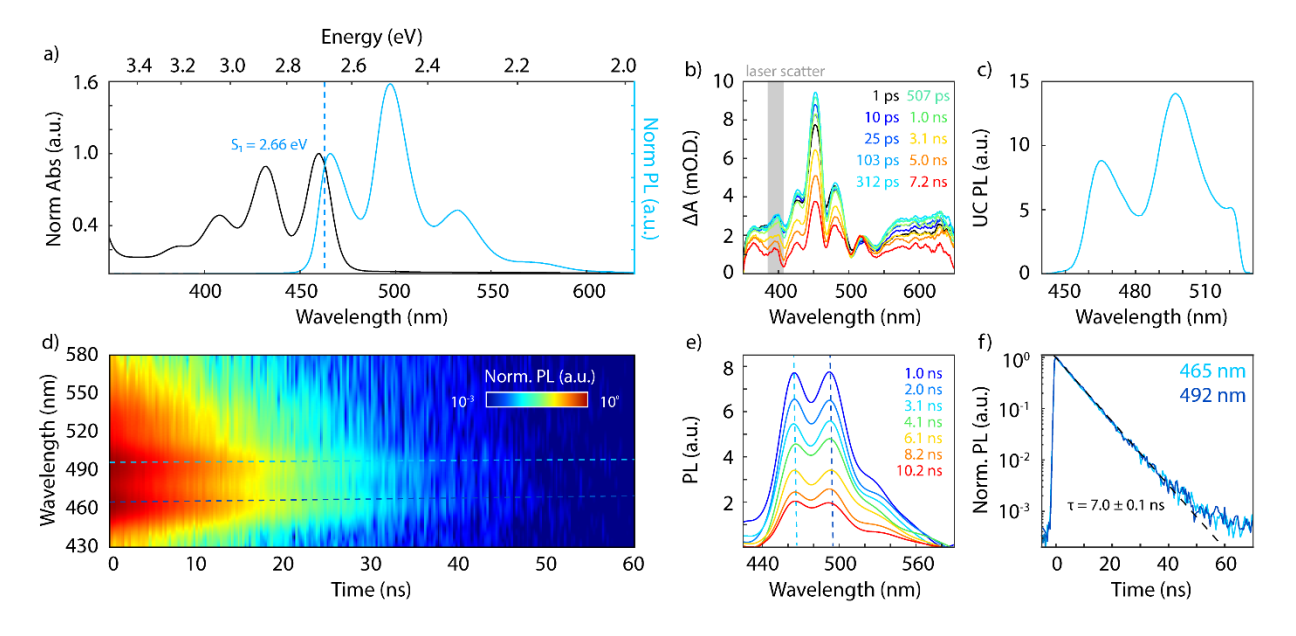


Figure 1: a) Normalized absorption (black) and PL (blue) spectra of a NaPy in toluene (150 μ M) with the extracted S_1 energy highlighted. b) TA spectra extracted at specific delay times for the NaPy solution under 400 nm pump at 1.33 mJ cm². The grey box denotes excess laser scattering. c) Upconverted PL of the NaPy/ZnOEP solution (532 nm, 15 mW cm²). d) Time-resolved emission (TRES) map of the NaPy solution under 405 nm excitation at a repetition rate of 1 MHz. e) PL spectra extracted at certain delay times; two spectral features 465 (light blue) and 492 nm (dark blue) are highlighted by the dashed lines. f) PL decays for the 465 (light blue) and 492 nm (dark blue) features and the extracted lifetime τ .

Having demonstrated successful UC in solution, solid-state NaPy OSC thin films as well as lead halide perovskite bilayer thin films consisting of the methylammonium-free 9% cesium 91% formamidinium lead triiodide perovskite (Cs_{0.09}FA_{0.91}PbI₃, CsFA) to increase long-term device stability are fabricated.^{35–38} The absorption spectrum of the solid-state NaPy OSC film in Figure 2a shows the expected slightly red-shifted

vibronic transitions with respect to the solution spectra shown previously in Figure 1, as well as an additional pronounced red-shifted aggregate-related absorption feature with higher oscillator strength, which is in agreement with the previously reported J-type aggregation of this material.²⁷ The corresponding solid-state PL spectrum of NaPy under 405 nm excitation surprisingly is made up of two distinct transitions: 1) the expected emission (~ 520 nm, 2.38 eV) from an amorphous NaPy thin film, with slightly redshifted features due to changes in the effective dielectric environment and the first vibronic transition (0 - 0) diminished in contrast to solution due to intermolecular interactions and reabsorption effects.^{39,40} 2) A weaker redshifted aggregate-related emission feature (~ 620 nm, 2.0 eV) that was not previously present in solution (compare Figure 1a) and has not previously been reported for this molecule. Extraction of the singlet state energy based on the overlap between the absorption and emission spectrum analogous to the previous solution measurement yields $S_1 = 2.39$ eV. However, if the two observed emissive states are viewed as discrete states, a singlet energy S_1 = 2.51 eV is extracted for the molecular emission, while the singlet energy for the aggregate state is S_1 = 2.15 eV.

To highlight the fact that these states are indeed discrete and not directly coupled, time-resolved emission spectroscopy (TRES) is used. Figure 2b-d emphasizes the differences in the PL lifetime of these two features. The PL spectra at selected decay times show that within the instrument response function of our setup (~ 0.3 ns) both states are populated and the lower energy feature S_1 " is not populated indirectly through slow energy transfer from the high energy S_1 . However, spectral slices indicate that at early times, the emission primarily stems from the amorphous molecular environment, while the delayed fluorescence (t > 3 ns) is dominated by emission from the aggregate state (Figure 2c). The bright PL at 520 nm decays with an early lifetime of $\tau = 0.7$ ns and with a power law dependence ($t^{-0.92}$) at later times which has been attributed to geminate fusion of the associated triplet pair state $^{1}(TT)$ and the separated triplet pair state (T...T). 34,41,42 while the redshifted aggregate-induced emission at 620 nm is long-lived and decays triexponentially with $\tau_{ave} = 5.9$ ns (Figure 2d), which is not in agreement with the high oscillator strength and fast lifetimes commonly associated with J-aggregates. Interestingly, the considerable Stokes shift (0.42 eV) of this aggregate-induced emission and long emission lifetime, shown in Figure 2d, are in contrast to

the expected properties of a J-aggregate,⁴³ and are closer in property to *e.g.*, an excimer state^{13,44–48} or a strongly coupled J-dimer.³⁹ This may indicate that the aggregate state is not directly emitting, rather emission occurs after internal conversion to another state, such as the 'dull' state proposed by Schmidt and coworkers in tetracene thin films.⁴⁹ As a result, here, we refrain from referring to this aggregate state directly as a J-aggregate and just consider it as an aggregation-related feature until the precise nature has been unraveled. Additional studies will be of interest in the future to clearly elucidate the complex underlying photophysics of the NaPy molecule and aggregate states.

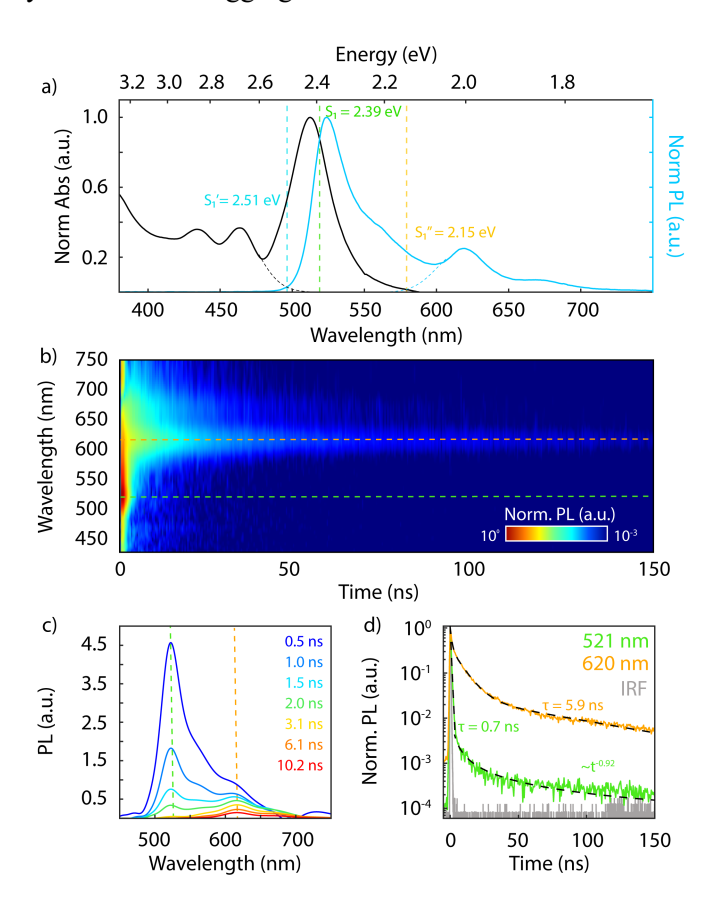


Figure 2: a) Solid-state absorption (black) and PL (blue) of the NaPy OSC film with the different possible S_1 energies highlighted. The dashed lines are Gaussian fits to the absorption and PL for extrapolation of S_1 ' and S_1 ''. b) TRES map of the NaPy OSC under 405 nm excitation at a repetition rate of 1 MHz. c) Spectra at specific time points extracted from the TRES map, where spectral features at 521 nm (green) and 620 nm (orange) are highlighted by the dashed lines. d) PL decays for the 521 nm (green) and 620 nm (orange) spectral features with the associated PL lifetimes. The instrument response function (IRF) is shown in grey.

To unravel the cause of the different emissive states in NaPy in more detail, we change the local environment of the NaPy molecules by fabricating samples with different degrees of crystallinity to investigate its role on the emissive properties in more detail. For the smooth OSC thin films presented thus

far, the emission from the molecular state at 521 nm dominates the emission spectrum (Figure 3, top). This is in agreement with a largely amorphous film, where intermolecular interactions are weak, and little longrange molecular order is present. When an OSC film with larger crystallites is formed from a saturated NaPy solution, two distinct emission spectra are found. In the amorphous regions between crystallites, the PL spectrum corresponding to amorphous NaPy is found, while on the crystallites, the red-shifted aggregate emission is increased in intensity (Figure 3, middle) and the high energy region is reduced in intensity. Lastly, a macroscopic NaPy crystal is grown, which exhibits strong emission from the red-shifted aggregate feature (Figure 3, bottom). However, when considering the lower brightness of the aggregate state, it becomes apparent that the aggregate state dominates the optical properties of the ordered crystal. All emission spectra can be fit to four Gaussians, indicating that the same optical transitions are present for each crystalline environment. While reabsorption effects and inner filtering must be considered when interpreting the relative PL intensity, ^{39,40} these cannot be the underlying cause of the shift in the emission spectra and change in the branching ratio between the emissive states. Figure 2 indicates minimal overlap of the absorption/scattering onset with any emission features at wavelengths longer than 550 nm, hence only the first vibronic transition (0-0) would be strongly affected. Hence, the inner filtering effect can only explain the reduction in PL intensity and slight redshift for the first vibronic feature in the more strongly scattering crystalline environments, but not the increased redshifted emission for the crystal (compare Table 1 for a summary of the extracted parameters).

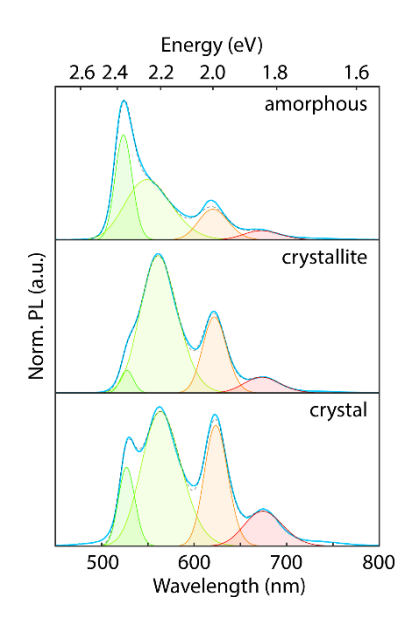


Figure 3: Gaussian fits (green, orange, to the PL spectra (blue lines) for the amorphous (top) and crystallite (middle) NaPy thin films and macroscopic NaPy crystal (bottom). The dashed line represents the sum of the individual Gaussian fits.

Table 1: Summary of the photophysical properties of NaPy in solid state and in solution.

NaPy	λ_{abs} (nm)			$\lambda_{PL}(nm)$				$\lambda_{UCPL}(nm)$		τ (ns)	
Solution (toluene)	407	432	460	465	492	532	575	465	497	7	
Amorphous	434	463	512	521	560	620	675			521 nm	620 nm
Crystallite				528	561	622	675	523	620	$\tau = 0.7$ $\propto t^{-0.92}$	$\tau = 5.9$
Crystal				530	560	622	675				

Lastly, the properties of NaPy as a solid-state annihilator when interfaced with the perovskite triplet sensitizer are investigated. Figure 4a shows the emission of the CsFA/NaPy bilayer device under 405 nm excitation. As expected, the NaPy emission features for both the molecular and aggregate emission are found, as well as the residual perovskite emission. However, under 780 nm excitation, where only the perovskite is excited and emission from NaPy stems from the TTA-UC process, the emission spectrum is considerably different (Figure 4b). The high-energy emission is reduced in intensity while the low-energy PL at 620 nm is strongly enhanced. In addition, the first vibronic feature of the upconverted PL at 520 nm is enhanced in comparison to the direct PL. However, as emphasized previously, the emission spectrum and branching ratio between multiple emissive states should not be sensitive to the process by which the singlet state is accessed, unless the true singlet state is not actually reached in the UC process or a different OSC

population is emitting under the different conditions. To further show the changes present between direct excitation and upconversion, the upconverted emission spectrum is normalized by the emission under direct excitation (Figure 4c). The upconversion efficiency η_{UC} is proportional to the triplet generation efficiency (η_{ET}) , the efficiency of TTA (η_{TTA}) , as well as the quantum yield of NaPy (η_{QY}) :

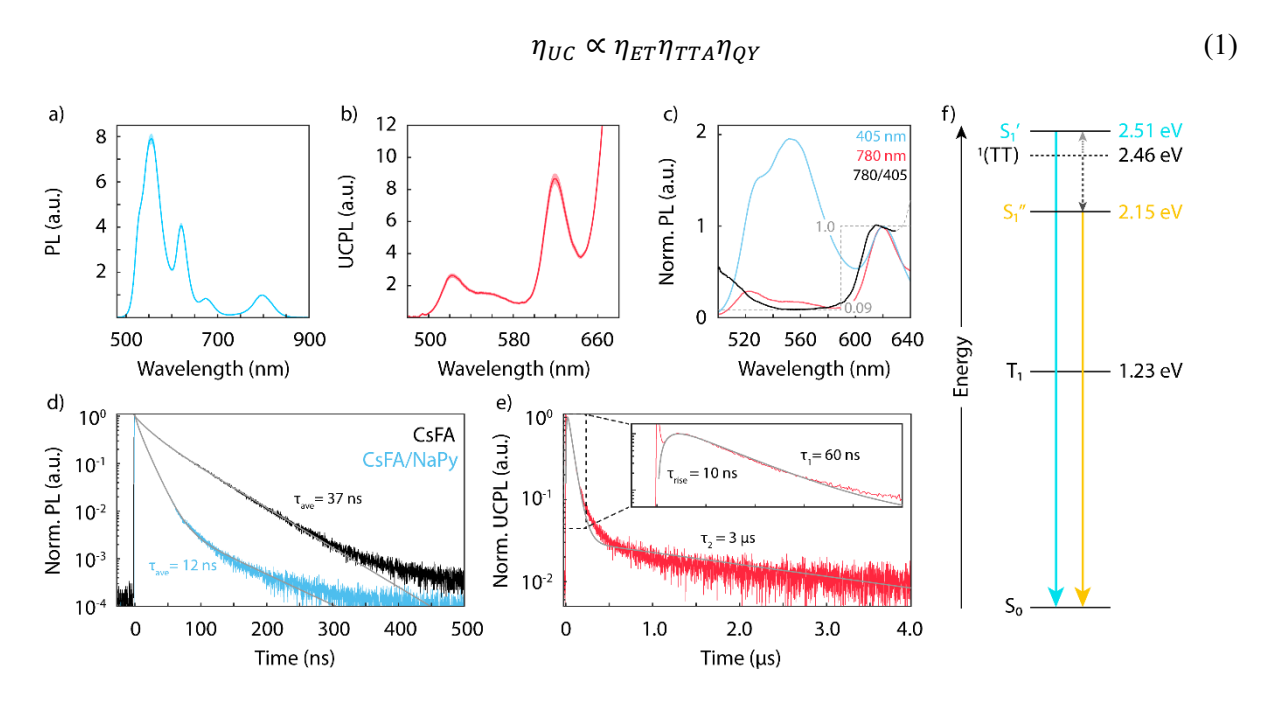


Figure 4: a) Average steady-state PL spectrum of the CsFA/NaPy bilayer film under 405 nm (30 W cm⁻²) excitation across four different spots. The shaded region represents the 95% confidence interval, indicating a homogeneous emission spectrum across the sample. b) Average UCPL spectrum of the CsFA/NaPy bilayer under 780 nm (153 W cm⁻²) excitation across ten spots. The shaded region represents the 95% confidence interval. c) Ratio of NaPy spectral features (black) under 405 nm (blue) and 780 nm (red) excitations normalized to the 620 nm aggregate PL feature. d) Perovskite PL decays for the CsFA and CsFA/NaPy films under 780 nm excitation (81 mW cm⁻²). Triexponential fits (grey) and amplitude weighted lifetimes are included for both films. e) UCPL dynamics of the CsFA/NaPy bilayer under 780 nm excitation measured at 250 kHz (175 mW cm⁻²). The corresponding fit (grey) and lifetimes of the singe rising exponential, and two decaying exponentials are included. The inset highlights the early rise and decay. The immediate spike in intensity is due to a small amount of overlapping perovskite PL. f) Proposed energy diagram for the different states present within NaPy.

By removing the impact of the direct emission intensity ($\propto \eta_{QY}$), *i.e.*, accounting for the much higher emission yield from the high energy state S_1 ', this normalization emphasizes the ratio of the upconverted photons stemming from each distinct state. The low energy aggregate-based state is clearly dominating the emission spectrum, with a ratio of 1:0.09 (aggregate:direct emission). However, it is not yet clear whether this effect is caused by the charge extraction step at the perovskite/NaPy interface, or if the triplet diffusion and annihilation rates are improved in the aggregate due to increased electronic coupling, or whether the

lowering of the singlet energy in the aggregate results in preferential TTA-UC to the aggregate singlet energy level (S_1 "= 2.15 eV) due to the increased energetic driving force since $E(S_1") < 2 E(T_1)$.

The PL decays of the CsFA perovskite and bilayer films shown in Figure 4d follow the same trend as previously established for both the state-of-the-art rubrene system and newer 1-CBPEA system, where charge extraction at the perovskite/OSC interface results in quenching of the perovskite lifetime. ^{12,21} Investigations into the upconverted dynamics, however, show clear similarities to the 1-CBPEA system and stark differences to the rubrene UC system: a single rapid rise of $\tau_{rise} = 10$ ns is found and within the time window of 4 μ s, the UCPL has nearly decayed entirely. Comparison of the CsFA/NaPy bilayer perovskite lifetime of $\tau_{ave} = 12$ ns rules out its contribution to the longer-lived decay observed in the UCPL on the order of 3 μ s. However, this is only a lower bound for the triplet lifetime, as previous studies have shown that the repetition rate can influence the extracted triplet lifetime. ^{7,9}

Lastly, the results are put into context with the previously suggested causes for the differences in the PL spectra under direct excitation or after upconversion. Since no distinct changes in the perovskite PL lifetimes are found across a sample, and the same spot shows a different PL spectrum under 405 and 780 nm excitation, differences in charge extraction are ruled out as the underlying cause. While increased coupling and triplet diffusion within the aggregate may indeed play an underlying role, if the singlet energy achieved after TTA-UC is equal to the same S₁ state that is directly excited, we would still expect the same branching ratio between the emissive states as under direct excitation.

Hence, we propose that the aggregation-related lowering of the singlet excited state changes the fundamental energy landscape such that the triplet pair state $^{1}(TT)$ formed during TTA-UC is straddled by the higher energy molecular singlet energy level S_{1} ' and the lower aggregate singlet energy S_{1} " (Figure 4e). As a result, conversion of $^{1}(TT)$ to S_{1} " = 2.15 eV will occur rapidly and with higher efficiency since the process is exothermic, while the conversion of $^{1}(TT)$ to S_{1} " = 2.51 eV is slightly endothermic. Considering Aggarwal's triplet energy assignment for NaPy in solid state: $T_{1} = 1.23$ eV, 27 this places $^{1}(TT)$ at 2.46 eV,

50 meV below S_1 ', an energy barrier that can be slowly overcome with ambient thermal energy, but with lower efficiency than the exothermic depopulation pathway to S_1 ''.

CONCLUSION

In conclusion, the results presented here highlight the critical role of the underlying crystal structure and resultant intermolecular electronic coupling on the energy landscape underlying TTA-UC and the reverse process of singlet fission. Furthermore, this study indicates that aggregation-related effects can not only be used as leverage to influence the efficiency and rate of TTA-UC, but also be used as a feature to turn on the process of TTA-UC in singlet fission materials by modifying the underlying energy landscape. This result has the potential to reshape the experimental approach to finding new compatible annihilators for solid-state UC.

The key to unlocking TTA-UC will be to fundamentally understand the photophysical properties of not only the OSC monomers, but their ensemble properties stemming from intermolecular interactions on the nanoscale to the macroscale and on timescales ranging from femtoseconds to milliseconds. Albeit beyond the scope of this initial study, future studies that spatially and spectrally resolve and pinpoint the nature of the underlying emissive states in NaPy will be of interest.

EXPERIMENTAL METHODS

Device Synthesis

For the bilayer and OSC thin films, glass substrates were cleaned *via* sonication for 15 min in each of the following: 2% Hellmanex, deionized water, ethanol, and acetone. After sonication, the substrates were cleaned by UV-ozone (Ossila) treatment for 15 min. Precursor solutions of PbI₂ (1.2 M, TCI), CsI (1.2 M, 99.999% Sigma), and FAI (1.2 M, Dyenamo) were prepared in anhydrous DMF:DMSO (9:1 v/v Sigma-Aldrich) in a 1:1.09 ratio. The precursor solution was diluted to 0.6 M prior to spin-coating at 1000 rpm for 10 s then 5000 rpm for 30 s. Anhydrous chlorobenzene (Sigma-Aldrich) was used as the antisolvent. The films were annealed at 120 °C for 45 min prior to solvent treatment (5 s) with acetonitrile (Sigma-Aldrich).²¹

Naphtho[2,3-a]pyrene (NaPy, 98.0%, TCI) was used without further purification. A saturated 10 mg mL⁻¹ solution of NaPy in anhydrous toluene (Sigma-Aldrich) was prepared then spin-coated onto the perovskite substrates at 6000 rpm for 20 s and annealed at 100 °C for 1 min. OSC only films were made by spin-coating NaPy onto bare glass substrates. The 'amorphous' NaPy films were fabricated with the clear supernatant, while 'crystallite' films were formed after vigorous stirring of the saturated solution to include undissolved NaPy crystallites. Films were encapsulated with a glass cover slip using a two-part epoxy (Devcon) under an inert nitrogen atmosphere (<0.5 ppm O₂).

Crystal Growth

NaPy crystals were grown in air-free atmosphere (<0.5 ppm O_2) through an anti-solvent diffusion method. In a small vial, 70 μ L of the 10 mg mL⁻¹ NaPy stock was diluted with 470 μ L of anhydrous toluene (Sigma) then placed uncapped into a larger vial of an ethanol:toluene (1:1, v/v, Sigma) mixture which was then capped and left undisturbed until the crystal formed.

Solution Upconversion

All materials were prepared in an air-free environment (<0.5 ppm of O_2). Zinc (II) octaethylporyphrin (ZnOEP) (97%, Sigma) was used without further purification. Stock solution of ZnOEP and NaPy were made by diluting with anhydrous toluene (Sigma). Upconverting solutions contained 7.7 μ M ZnOEP and 7.25 μ L of the 10 mg mL⁻¹ NaPy stock solution diluted to 400 μ L with toluene. Solutions were transferred to quartz cuvettes for characterization.

Steady-State Characterizations

Visible absorption spectra were collected with a Thermo Scientific Evolution 220 spectrophotometer.

Steady-state PL spectra were collected by an Ocean Optics spectrometer (HR2000+ES) in a homebuilt setup. Direct excitation emission for the thin films and solutions were collected *via* a 405 nm continuous wave laser (LDH-D-C-405, PicoQuant) at a 30 W cm⁻² where excess laser scatter was removed *via* a 425 long-pass filter (Chroma Tech.). The NaPy single crystal direct emission was collected under 405 nm continuous wave at 542 W cm⁻².

Upconverted emission for the NaPy:ZnOEP solution was collected using a 532 nm pulsed (LDH-P-FA-530L, PicoQuant) at a repetition frequency of 80 MHz and 15 W cm⁻². Laser scatter was removed with a 532 nm notch filter (Thorlabs). For the bilayer films, a 780 nm continuous wave laser (LDH-D-C-780, PicoQuant) was used at 152 W cm⁻² where a 700 nm short-pass filter (Thorlabs) was used to isolate the upconverted signal.

Time-Resolved Emission Spectroscopy (TRES)

Time-resolved PL measurements for the perovskite PL decays were collected under 780 nm picosecond pulsed excitation (LDH-D-C-780, PicoQuant) at 125 kHz with at a power density of 81 mW cm⁻². An 800 nm long-pass filter (Thorlabs) and 780 nm notch filter (Thorlabs) were used to isolate the perovskite emission and minimize laser scattering. Upconverted PL decays were measured under 780 nm picosecond pulsed excitation (LDH-D-C-780, PicoQuant) at 250 kHz with a power density of 175 mW cm⁻². A 650 nm short pass (Thorlabs) filter was used to isolate the upconverted emission and remove excess laser scattering. The single photon counting avalanche photodiode used is from Micro Photon Devices, and all collected PL decays was histogrammed by a MultiHarp 150 TCSPC unit from PicoQuant.

Wavelength-dependent PL maps were collected using a Gemini interferometer (NIREOS) for both the NaPy solution and OSC measurements. TRES maps for the solution measurement were recorded over 180 steps from 425 to 660 nm at, and 233 steps with a spectral range of 425 to 700 nm for the NaPy OSC measurement. Both were integrated for 15001 ms. A 405 nm picosecond pulsed laser diode (PicoQuant LDH-D-C-405) was used at a repetition frequency of 1 MHz at a power density of 2.9 mW cm⁻² for the solution and 98 mW cm⁻² for the OSC. Photon arrival times were collected *via* a silicon single-photon avalanche photodiode (Micro Photon Devices SPD-100-C0C) connected to a HydraHarp 400 (PicoQuant) event timer. A 425 nm long pass filter (Chroma Tech.) was used to remove excess laser scatter.

Ultrafast Transient Absorption

Transient absorption (TA) measurements were taken using a HELIOS Fire transient absorption spectrometer (Ultrafast Systems). An Astrella-V-F-1K amplifier was used to generate femtosecond laser pulses where the Vitara-S Coherent Ti:Sapphire laser used was amplified using a 1 kHz Coherent

Revolution-50 pump laser. The resulting laser pulses were 5 mJ with a full width half max of 100 fs at 800

nm. Pump and probe beams were directed through an optical parametric amplifier (OperaA Solo, Coherent)

and delay stage, respectively. The white light continuum was generated via a CaF₂ crystal (320 nm to 650

nm). Excess laser scattering was minimized through a dual chopper system, and neutral density filters were

used to attenuate pump power. For all measurements, three spectra were collected with a 0.5 s integration

time at each delay position with an exponential point collection method starting at 0.01 ps, resulting in a

total of 200 points. A 400 nm pump was used at a power density of 1.33 mJ cm⁻². The TA maps were

processed through the Surface Xplorer software package from Ultrafast Systems in addition to MATLAB.

ASSOCIATED CONTENT

Data Availability

Raw data files are available at DOI: 10.17605/OSF.IO/P3TE5.

AUTHOR INFORMATION

Corresponding Author

*E-mail: lnienhaus@fsu.edu

Notes

The authors declare no conflict of interest.

ACKNOWLEDGEMENTS

The authors thank Rachel Weiss Clark for supporting measurements. This work was supported by the

National Science Foundation under Grant No. DMR-2237977. We thank the Camille and Henry Dreyfus

Foundation (TC-23-050) for support. The authors acknowledge additional support by Florida State

University. This project used resources provided by the Materials Characterization Laboratory

(FSU075000MAC) at the FSU Department of Chemistry and Biochemistry. Ultrafast transient absorption

15

measurements were performed on a spectrometer supported by the National Science Foundation under Grant No. CHE-1919633.

REFERENCES

- (1) Sullivan, C. M.; Nienhaus, L. Generating Spin-Triplet States at the Bulk Perovskite/Organic Interface for Photon Upconversion. *Nanoscale* **2023**, *15* (3), 998–1013. https://doi.org/10.1039/D2NR05767K.
- (2) Conti, C. R.; Bieber, A. S.; VanOrman, Z. A.; Moller, G.; Wieghold, S.; Schaller, R. D.; Strouse, G. F.; Nienhaus, L. Ultrafast Triplet Generation at the Lead Halide Perovskite/Rubrene Interface. *ACS Energy Lett.* **2022**, *7* (2), 617–623. https://doi.org/10.1021/acsenergylett.1c02732.
- (3) Wieghold, S.; Bieber, A. S.; VanOrman, Z. A.; Daley, L.; Leger, M.; Correa-Baena, J.-P.; Nienhaus, L. Triplet Sensitization by Lead Halide Perovskite Thin Films for Efficient Solid-State Photon Upconversion at Subsolar Fluxes. *Matter* **2019**, *1* (3), 705–719. https://doi.org/10.1016/j.matt.2019.05.026.
- (4) Prashanthan, K.; Naydenov, B.; Lips, K.; Unger, E.; MacQueen, R. W. Interdependence of Photon Upconversion Performance and Antisolvent Processing in Thin-Film Halide Perovskite-Sensitized Triplet—Triplet Annihilators. *J. Chem. Phys.* **2020**, *153* (16), 164711. https://doi.org/10.1063/5.0026564.
- (5) VanOrman, Z. A.; Nienhaus, L. Bulk Metal Halide Perovskites as Triplet Sensitizers: Taking Charge of Upconversion. *ACS Energy Lett.* **2021**, *6* (10), 3686–3694. https://doi.org/10.1021/acsenergylett.1c01794.
- (6) Nienhaus, L.; Wu, M.; Geva, N.; Shepherd, J. J.; Wilson, M. W. B.; Bulović, V.; Van Voorhis, T.; Baldo, M. A.; Bawendi, M. G. Speed Limit for Triplet-Exciton Transfer in Solid-State PbS Nanocrystal-Sensitized Photon Upconversion. *ACS Nano* 2017, *11* (8), 7848–7857. https://doi.org/10.1021/acsnano.7b02024.
- (7) Wu, M.; Congreve, D. N.; Wilson, M. W. B.; Jean, J.; Geva, N.; Welborn, M.; Van Voorhis, T.; Bulović, V.; Bawendi, M. G.; Baldo, M. A. Solid-State Infrared-to-Visible Upconversion Sensitized by Colloidal Nanocrystals. *Nat. Photonics* **2016**, *10* (1), 31–34. https://doi.org/10.1038/nphoton.2015.226.
- (8) Wieghold, S.; Bieber, A. S.; VanOrman, Z. A.; Rodriguez, A.; Nienhaus, L. Is Disorder Beneficial in Perovskite-Sensitized Solid-State Upconversion? Role of DBP Doping in Rubrene. *J. Phys. Chem. C* **2020**, *124* (33), 18132–18140. https://doi.org/10.1021/acs.jpcc.0c05290.
- (9) Wieghold, S.; Bieber, A. S.; VanOrman, Z. A.; Nienhaus, L. Influence of Triplet Diffusion on Lead Halide Perovskite-Sensitized Solid-State Upconversion. *J. Phys. Chem. Lett.* **2019**, 3806–3811. https://doi.org/10.1021/acs.jpclett.9b01526.
- (10) Wieghold, S.; Nienhaus, L. Precharging Photon Upconversion: Interfacial Interactions in Solution-Processed Perovskite Upconversion Devices. *J. Phys. Chem. Lett.* **2020**, *11* (3), 601–607. https://doi.org/10.1021/acs.jpclett.9b03596.
- (11) Wang, L.; Yoo, J. J.; Lin, T.-A.; Perkinson, C. F.; Lu, Y.; Baldo, M. A.; Bawendi, M. G. Interfacial Trap-Assisted Triplet Generation in Lead Halide Perovskite Sensitized Solid-State Upconversion. *Adv. Mater.* **2021**, *33* (27), 2100854. https://doi.org/10.1002/adma.202100854.
- (12) Sullivan, C. M.; Nienhaus, L. Recharging Upconversion: Revealing Rubrene's Replacement. *Nanoscale* **2022**, *14* (46), 17254–17261. https://doi.org/10.1039/D2NR05309H.
- (13) Nandi, A.; Manna, B.; Ghosh, R. Interplay of Exciton–Excimer Dynamics in 9,10–Diphenylanthracene Nanoaggregates and Thin Films Revealed by Time-Resolved Spectroscopic Studies. *Phys. Chem. Chem. Phys.* **2019**, *21* (21), 11193–11202. https://doi.org/10.1039/C9CP01124B.

- (14) Ishwara, T.; Feng, J.; de Clercq, D. M.; Geng, R.; Alves, J.; McCamey, D. R.; Nielsen, Michael. P.; Schmidt, T. W. Nanoporous Solid-State Sensitization of Triplet Fusion Upconversion. *ACS Energy Lett.* **2023**, 4078–4084. https://doi.org/10.1021/acsenergylett.3c01678.
- (15) Gao, C.; Zhang, B.; Hall, C. R.; Li, L.; Chen, Y.; Zeng, Y.; Smith, T. A.; Wong, W. W. H. Triplet Fusion Upconversion Using Sterically Protected 9,10-Diphenylanthracene as the Emitter. *Phys. Chem. Chem. Phys.* **2020**, *22* (11), 6300–6307. https://doi.org/10.1039/C9CP06311K.
- (16) Enomoto, R.; Hoshi, M.; Oyama, H.; Agata, H.; Kurokawa, S.; Kuma, H.; Uekusa, H.; Murakami, Y. Van Der Waals Solid Solution Crystals for Highly Efficient In-Air Photon Upconversion under Subsolar Irradiance. *Mater. Horiz.* 2021, 8 (12), 3449–3456. https://doi.org/10.1039/D1MH01542G.
- (17) de Clercq, D. M.; Yang, J.; Hanif, M.; Alves, J.; Feng, J.; Nielsen, M. P.; Kalantar-Zadeh, K.; Schmidt, T. W. Exciton Dissociation, Charge Transfer, and Exciton Trapping at the MoS2/Organic Semiconductor Interface. *J. Phys. Chem. C* **2023**, *127* (23), 11260–11267. https://doi.org/10.1021/acs.jpcc.3c01682.
- (18) Akbulatov, A. F.; Ustinova, M. I.; Gutsev, L.; Tsarev, S. A.; Dremova, N. N.; Zhidkov, I.; Luchkin, S. Yu.; Ramachandran, B. R.; Frolova, L.; Kurmaev, E. Z.; Stevenson, K. J.; Aldoshin, S. M.; Troshin, P. A. When Iodide Meets Bromide: Halide Mixing Facilitates the Light-Induced Decomposition of Perovskite Absorber Films. *Nano Energy* **2021**, *86*, 106082. https://doi.org/10.1016/j.nanoen.2021.106082.
- (19) Valle-Pulido, J.; Solis, O. E.; Esparza, D.; Arturo Rodríguez-Rojas, R.; Turren-Cruz, S.-H.; Rivas, J. M.; Zarazúa, I. Degradation Analysis of Perovskite Solar Cells Doped with MABr3 via Electrochemical Impedance. *Sol. Energy* **2023**, *258*, 148–155. https://doi.org/10.1016/j.solener.2023.04.058.
- (20) Boldyreva, A. G.; Zhidkov, I. S.; Tsarev, S.; Akbulatov, A. F.; Tepliakova, M. M.; Fedotov, Y. S.; Bredikhin, S. I.; Postnova, E. Y.; Luchkin, S. Y.; Kurmaev, E. Z.; Stevenson, K. J.; Troshin, P. A. Unraveling the Impact of Hole Transport Materials on Photostability of Perovskite Films and p—i—n Solar Cells. *ACS Appl. Mater. Interfaces* **2020**, *12* (16), 19161–19173. https://doi.org/10.1021/acsami.0c01027.
- (21) Sullivan, C. M.; Bieber, A. S.; Drozdick, H. K.; Moller, G.; Kuszynski, J. E.; VanOrman, Z. A.; Wieghold, S.; Strouse, G. F.; Nienhaus, L. Surface Doping Boosts Triplet Generation Yield in Perovskite-Sensitized Upconversion. *Adv. Opt. Mater.* 2023, *11* (1), 2201921. https://doi.org/10.1002/adom.202201921.
- (22) France, C. B.; Parkinson, B. A. Naphtho[2,3-a]Pyrene Forms Chiral Domains on Au(111). *J. Am. Chem. Soc.* **2003**, *125* (42), 12712–12713. https://doi.org/10.1021/ja0370560.
- (23) France, C. B.; Parkinson, B. A. Chiral Morphologies and Interfacial Electronic Structure of Naphtho[2,3-a]Pyrene on Au(111). *Langmuir* **2004**, *20* (7), 2713–2719. https://doi.org/10.1021/la035532i.
- (24) Iski, E. V.; Jewell, A. D.; Tierney, H. L.; Kyriakou, G.; Sykes, E. C. H. Organic Thin Film Induced Substrate Restructuring: An STM Study of the Interaction of Naphtho[2,3-a]Pyrene Au(111) Herringbone Reconstruction. *J. Vac. Sci. Technol. A* **2011**, *29* (4), 040601. https://doi.org/10.1116/1.3602072.
- (25) Jarikov, V. V. Improving Operating Lifetime of Organic Light-Emitting Diodes with Polycyclic Aromatic Hydrocarbons as Aggregating Light-Emitting-Layer Additives. *J. Appl. Phys.* **2006**, *100* (1), 014901. https://doi.org/10.1063/1.2214535.
- (26) Kwon, J.; Hong, J.-P.; Lee, W.; Noh, S.; Lee, C.; Lee, S.; Hong, J.-I. Naphtho[2,3,a]Pyrene as an Efficient Multifunctional Organic Semiconductor for Organic Solar Cells, Organic Light-Emitting Diodes, and Organic Thin-Film Transistors. *Org. Electron.* **2010**, *11* (6), 1103–1110. https://doi.org/10.1016/j.orgel.2010.03.017.
- (27) Aggarwal, N.; Patnaik, A. Dimeric Conformation Sensitive Electronic Excited States of Tetracene Congeners and Their Unconventional Non-Fluorescent Behaviour. *J. Chem. Sci.* **2019**, *131* (6), 52. https://doi.org/10.1007/s12039-019-1626-5.

- (28) Cheng, Y. Y.; Fückel, B.; Khoury, T.; Clady, R. G. C. R.; Ekins-Daukes, N. J.; Crossley, M. J.; Schmidt, T. W. Entropically Driven Photochemical Upconversion. *J. Phys. Chem. A* **2011**, *115* (6), 1047–1053. https://doi.org/10.1021/jp108839g.
- (29) He, S.; Han, Y.; Guo, J.; Wu, K. Entropy-Powered Endothermic Energy Transfer from CsPbBr3 Nanocrystals for Photon Upconversion. *J. Phys. Chem. Lett.* **2022**, *13* (7), 1713–1718. https://doi.org/10.1021/acs.jpclett.2c00088.
- (30) Gray, V.; Dreos, A.; Erhart, P.; Albinsson, B.; Moth-Poulsen, K.; Abrahamsson, M. Loss Channels in Triplet–Triplet Annihilation Photon Upconversion: Importance of Annihilator Singlet and Triplet Surface Shapes. *Phys. Chem. Chem. Phys.* **2017**, *19* (17), 10931–10939. https://doi.org/10.1039/C7CP01368J.
- (31) Lai, H.; Zhao, T.; Deng, Y.; Fan, C.; Wu, W.; Yang, C. Assembly-Enhanced Triplet-Triplet Annihilation Upconversion in the Aggregation Formed by Schiff-Base Pt(II) Complex Grafting-Permethyl-β-CD and 9, 10-Diphenylanthracence Dimer. *Org. Polym. Lumin. Mater.* **2019**, *30* (11), 1979–1983. https://doi.org/10.1016/j.cclet.2019.09.009.
- (32) Levine, A. M.; He, G.; Bu, G.; Ramos, P.; Wu, F.; Soliman, A.; Serrano, J.; Pietraru, D.; Chan, C.; Batteas, J. D.; Kowalczyk, M.; Jang, S. J.; Nannenga, B. L.; Sfeir, M. Y.; R. Tsai, E. H.; Braunschweig, A. B. Efficient Free Triplet Generation Follows Singlet Fission in Diketopyrrolopyrrole Polymorphs with Goldilocks Coupling. *J. Phys. Chem. C* **2021**, *125* (22), 12207–12213. https://doi.org/10.1021/acs.jpcc.1c02737.
- (33) Piland, G. B.; Bardeen, C. J. How Morphology Affects Singlet Fission in Crystalline Tetracene. *J. Phys. Chem. Lett.* **2015**, *6* (10), 1841–1846. https://doi.org/10.1021/acs.jpclett.5b00569.
- (34) Bossanyi, D. G.; Sasaki, Y.; Wang, S.; Chekulaev, D.; Kimizuka, N.; Yanai, N.; Clark, J. In Optimized Rubrene-Based Nanoparticle Blends for Photon Upconversion, Singlet Energy Collection Outcompetes Triplet-Pair Separation, Not Singlet Fission. *J. Mater. Chem. C* **2021**. https://doi.org/10.1039/D1TC02955J.
- (35) Saliba, M.; Matsui, T.; Seo, J.-Y.; Domanski, K.; Correa-Baena, J.-P.; Nazeeruddin, M. K.; Zakeeruddin, S. M.; Tress, W.; Abate, A.; Hagfeldt, A.; Grätzel, M. Cesium-Containing Triple Cation Perovskite Solar Cells: Improved Stability, Reproducibility and High Efficiency. *Energy Environ. Sci.* **2016**, *9* (6), 1989–1997. https://doi.org/10.1039/C5EE03874J.
- (36) Kulbak, M.; Cahen, D.; Hodes, G. How Important Is the Organic Part of Lead Halide Perovskite Photovoltaic Cells? Efficient CsPbBr3 Cells. *J. Phys. Chem. Lett.* **2015**, *6* (13), 2452–2456. https://doi.org/10.1021/acs.jpclett.5b00968.
- (37) Yi, C.; Luo, J.; Meloni, S.; Boziki, A.; Ashari-Astani, N.; Grätzel, C.; Zakeeruddin, S. M.; Röthlisberger, U.; Grätzel, M. Entropic Stabilization of Mixed A-Cation ABX3 Metal Halide Perovskites for High Performance Perovskite Solar Cells. *Energy Environ. Sci.* **2016**, *9* (2), 656–662. https://doi.org/10.1039/C5EE03255E.
- (38) Lee, J.-W.; Kim, D.-H.; Kim, H.-S.; Seo, S.-W.; Cho, S. M.; Park, N.-G. Formamidinium and Cesium Hybridization for Photo- and Moisture-Stable Perovskite Solar Cell. *Adv. Energy Mater.* **2015**, *5* (20), 1501310. https://doi.org/10.1002/aenm.201501310.
- (39) Hestand, N. J.; Spano, F. C. Expanded Theory of H- and J-Molecular Aggregates: The Effects of Vibronic Coupling and Intermolecular Charge Transfer. *Chem. Rev.* **2018**, *118* (15), 7069–7163. https://doi.org/10.1021/acs.chemrev.7b00581.
- (40) Mukazhanova, A.; Trerayapiwat, K. J.; Mazaheripour, A.; Wardrip, A. G.; Frey, N. C.; Nguyen, H.; Gorodetsky, A. A.; Sharifzadeh, S. Accurate First-Principles Calculation of the Vibronic Spectrum of Stacked Perylene Tetracarboxylic Acid Diimides. *J. Phys. Chem. A* **2020**, *124* (16), 3055–3063. https://doi.org/10.1021/acs.jpca.9b08117.
- (41) Wolf, E. A.; Biaggio, I. Geminate Exciton Fusion Fluorescence as a Probe of Triplet Exciton Transport after Singlet Fission. *Phys. Rev. B* **2021**, *103* (20), L201201. https://doi.org/10.1103/PhysRevB.103.L201201.

- (42) Seki, K.; Sonoda, Y.; Katoh, R. Diffusion-Mediated Delayed Fluorescence by Singlet Fission and Geminate Fusion of Correlated Triplets. *J. Phys. Chem. C* **2018**, *122* (22), 11659–11670. https://doi.org/10.1021/acs.jpcc.8b02234.
- (43) Lim, S.-H.; Bjorklund, T. G.; Spano, F. C.; Bardeen, C. J. Exciton Delocalization and Superradiance in Tetracene Thin Films and Nanoaggregates. *Phys. Rev. Lett.* **2004**, *92* (10), 107402. https://doi.org/10.1103/PhysRevLett.92.107402.
- (44) Spano, F. C.; Silva, C. H- and J-Aggregate Behavior in Polymeric Semiconductors. *Annu. Rev. Phys. Chem.* **2014**, *65* (1), 477–500. https://doi.org/10.1146/annurev-physchem-040513-103639.
- (45) Deshmukh, A. P.; Koppel, D.; Chuang, C.; Cadena, D. M.; Cao, J.; Caram, J. R. Design Principles for Two-Dimensional Molecular Aggregates Using Kasha's Model: Tunable Photophysics in Near and Short-Wave Infrared. *J. Phys. Chem. C* **2019**, *123* (30), 18702–18710. https://doi.org/10.1021/acs.jpcc.9b05060.
- (46) Deshmukh, A. P.; Geue, N.; Bradbury, N. C.; Atallah, T. L.; Chuang, C.; Pengshung, M.; Cao, J.; Sletten, E. M.; Neuhauser, D.; Caram, J. R. Bridging the Gap between H- and J-Aggregates: Classification and Supramolecular Tunability for Excitonic Band Structures in Two-Dimensional Molecular Aggregates. *Chem. Phys. Rev.* **2022**, *3* (2), 021401. https://doi.org/10.1063/5.0094451.
- (47) Bricks, J. L.; Slominskii, Y. L.; Panas, I. D.; Demchenko, A. P. Fluorescent J-Aggregates of Cyanine Dyes: Basic Research and Applications Review. *Methods Appl. Fluoresc.* **2017**, *6* (1), 012001. https://doi.org/10.1088/2050-6120/aa8d0d.
- (48) Dimitriev, O. P.; Piryatinski, Y. P.; Slominskii, Y. L. Excimer Emission in J-Aggregates. *J. Phys. Chem. Lett.* **2018**, *9* (9), 2138–2143. https://doi.org/10.1021/acs.jpclett.8b00481.
- (49) Tayebjee, M. J. Y.; Clady, R. G. C. R.; Schmidt, T. W. The Exciton Dynamics in Tetracene Thin Films. *Phys. Chem. Chem. Phys.* **2013**, *15* (35), 14797–14805. https://doi.org/10.1039/C3CP52609G.

TOC Graphic

